IEEE Access
Multidisciplinary ⋮ Rapid Review ⋮ Open Access Journal

Received June 1, 2019, accepted June 24, 2019, date of publication June 28, 2019, date of current version July 15, 2019.

Digital Object Identifier 10.1109/ACCESS.2019.2925563

Graph-Regularized Laplace Approximation for Detecting Small Infrared Target Against Complex Backgrounds

FEI ZHOU, YIQUAN WU, YIMIAN DAI, PENG WANG, (Member, IEEE), AND KANG NI
College of Electronic and Information Engineering, Nanjing University of Aeronautics and Astronautics, Nanjing 211106, China

Corresponding author: Yiquan Wu (mltd2099@163.com)

This work was supported in part by the National Nature Science Foundation of China under Grant 61573183 and Grant 61801211, and in part by the Open Project Program of the National Laboratory of Pattern Recognition (NLPR) under Grant 201900029.

ABSTRACT Against complex background containing the tiny target, high-performance infrared small target detection is always treated as a difficult task. Many low-rank recovery-based methods have shown great potential, but they may suffer from high false or missing alarm when encountering the background with intricate interferences. In this paper, a novel graph-regularized Laplace low-rank approximation detecting model (GRLA) is developed for infrared dim target scenes. Initially, a non-convex Laplace low-rank regularizer instead of the nuclear norm is employed to boost the accuracy of heterogeneous background estimation. Then, to maintain the intrinsic structure between background patch-image, the graph regularization is incorporated in the detecting model. Besides, aiming at reducing the nontarget outliers, a reweighted l_1 norm with nonnegative constraint is used. Finally, the proposed model is extended to a generalized framework (G-GRLA) by replacing different non-convex rank functions. With the help of the alternating direction method of multiplier (ADMM), the solution of the proposed model is obtained by an iterative optimization scheme. The experimental results on extensive actual infrared images present the superior performance of our proposed method to compare with the state-of-the-art methods.

INDEX TERMS Small target detection, nonconvex low-rank regularizer, manifold information, graph regularization, reweighted l_1 norm with nonnegative constraint.

I. INTRODUCTION

Small infrared target detection, which aims to localize the suspicious incoming target from acquired infrared images, has aroused increasing attention as a key technology of infrared search and tracking applications (IRST). It has a wide range of applicability in plenty of military projects, such as automatic infrared target recognition, infrared guidance and antimissile [1]–[3]. However, suspicious projected targets generally present point-like structure at a far imaging distance, losing most of specific characteristics, such as detectable shape and texture. And the point target with concentrated brightness may be dispersed into blurred spots in unfavorable weather conditions, reducing target contrast. In addition, infrared image may be contaminated by the ambient noise and the inherent sensor factors. Moreover, small target would be immersed into clutter edges in sky scene, obscured by sea glint in oceanic background, or interfered by artificial building. Therefore, it is always a challenge and research hotspots to detect small target from complex infrared background.

Numerous advanced infrared small target detection methods have been proposed in recent years, which can be coarsely categorized into two groups, namely, multi-frame detection and single-frame detection. With some prior knowledge about target, such as shape and velocity, the multi-frame detection algorithms accomplish target detection task very well via the usage of spatial-temporal information in infrared sequences [4]. The state-of-the-art multi-frame detection algorithms include generalized likelihood ratio test [5],temporal profiles filtering [6], Markov random field [7], convolution neural network (CNN) [8], pipeline filtering [3] and so on. These approaches have achieved encouraging performance in the cases that background is assumed to be slowly

The associate editor coordinating the review of this manuscript and approving it for publication was Shuo Sun.

transitional and the target trajectory is regarded as consistent between adjacent frames [9]. However, when encountering high-speed targets like anti-ship missile, the background will change rapidly due to the fast motion between target and imaging device and the target continuity may be destroyed because of the jitter of the infrared sensing platform [10]. Their performance degrades seriously. For these reasons, the study of single-frame infrared small target detection is of great essential for practical IRST applications.

For the single-frame detection, conventional filtering methods [11]–[13] based on the assumption of background consistency are suitable for the simple homogeneous background but sensitive to the strong clutter and pixel-sized noise with high intensity in complex scenes. Under the hypothesis of regional saliency of target, saliency-based detection methods [14]–[20] delineate the dissimilarity between target and local area to characterize target singularity for highlighting target while neglecting background. However, these methods might be dull to target but sensitive to strong edges or target-like glint because the interferences may be more noticeable than real target with respect to the view of thermal brightness.

Recently, low-rank recovery theory [21] have been widely applied in image processing, such as object detection [22], background subtraction [23], image denoising [24]. Gao et al. [9] firstly quoted the theory to single-frame detection task under the prior assumptions of target sparsity and background nonlocal correlation. They proposed a representative work termed as Infrared Patch-Image (IPI) model, which transforms the small target detection task into a low-rank recovery problem [21]. The IPI model is formulated as:

$$\min_{\mathbf{L},\mathbf{S}} ||\mathbf{L}||_* + \lambda||\mathbf{S}||_1 \quad s.t. \quad \mathbf{D} = \mathbf{L} + \mathbf{S} \tag{1}$$

where the nuclear norm $||\cdot||_*$ as the background patch-image constraint is the sum of singular values of a matrix. $||\cdot||_1$ is the l_1-norm as regularization of target patch-image, and λ is a tradeoff between the low-rank and sparse components.

A. MOTIVATION

Although IPI model achieves promising detection performance in some scenarios, it still has some limitations when facing extremely heterogeneous backgrounds. At first, using the nuclear norm as the constraint of background patch-image leads to inexact estimation of background. The inherent reason lies in that the nuclear norm denotes the sum of all singular values rather than handling them equally as the matrix rank function does. It penalizes the larger singular value determining the background component more heavily than smaller ones, which will result in the absence of background information. Furthermore, the missing background information would be left in target image, becoming false alarm. In addition, although the way of using the sliding window raises the redundancy of the background features, it destroys the intrinsic structure of infrared image. Usually, the damage of the image structure will further deteriorate the recovery of the background. Finally, employing a constant tradeoff may be irrational since the invariable threshold rigidly deletes values less than itself. Therefore, under the scene with both highly complex background and less intensity target, an uncoordinated tradeoff would result in high false or missing alarm.

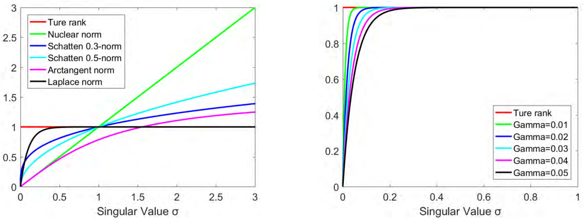

(a) (b)

FIGURE 1. Approximation of different non-convex rank function to the actual rank in terms of varying singular values.

To address the above drawbacks, we propose a novel small target detection model, named as graph-regularized Laplace low-rank approximation (GRLA). One of our main considerations is how to obtain an accurate background estimation under limited image patches. The larger singular values should be less penalized while the smaller ones should be more punished. In order to cater to the different punishment degree of singular values, we introduce a nonconvex low-rank regularizer called Laplace norm. Fig. 1 shows the advantage of Laplacian norm in approaching real rank compared with other rank functions. As shown in Fig. 1(a), the nuclear norm, arctangent rank function, Schatten 0.3-norm and Schatten 0.5-norm deviate significantly from the true rank when the singular values are larger than 1. By comparison, the Laplace norm (denoted by the black curve) fits the rank function better with the increase of singular values. In addition, the approximation quality can be adjusted by its parameter (as shown in Fig. 1(b)). Other one is that the manifold information is often used to preserve the intrinsic structure of low dimensional data [25]. How to explore the manifold information to preserve the background structure in small target detection problem is eagerly expected. Inspired by Ref. [26], graph regularization is exploited to constrain the background patch-image in our proposed model. Because the graph regularization as smooth operator can not only preserve the structure of background, but avoid introducing other interferences during the detection process. Finally, the sparse reweighted scheme is used to make the constant tradeoff adaptive. With the above considerations in mind, a novel single-frame small target detection framework is presented. The main contributions of the proposed model are summarized as three folds:

1) Laplace low-rank regularizer is introduced instead of the traditional nuclear norm. It can take unequal treatment to different rank component and achieve more complete background recovery. A sparse reweighted method is then used to adjust the tradeoff and eliminate the target-like false alarm in target image.

2) A nearest neighborhood graph regularization is constructed to preserve the inherent structure of patch-image.

Finally, the proposed method is extended to a generalized framework via using different nonconvex rank functions.

3) With the help of ADMM [27], an efficient algorithm is designed to solve the proposed method, in which the subproblem of nonconvex Laplace norm minimization is solved by recently developed generalized weight singular value threshold (WSVT) [28].

Extensive experiments on various real infrared images show outperforming performance of the proposed method compared with some state-of-art approaches in terms of quantitative indicators and subjective visual.

The remainder of the paper is organized as follows. In Section II, we review existing infrared small detection methods. Section III introduces the construction of the proposed method. Section IV gives the optimization of the proposed method and extends the method to a generalized model. Section V presents the experimental results. Section VI shows the discussion of parameter settings, algorithm convergence and complexity. In Section VII, we conclude this paper.

II. RELATED WORK

Recent years have witness great progress in infrared small target detection that covers two research interests: Track Before Detection (TBD) method and Detection Before Track (DBT) method. TBD methods can use the adjacent frame knowledge to enhance targets and suppress residual false alarm by using the spatial-temporal information in sequence image [5], [6]. Here, we will briefly go over the latter type of approaches, to which the proposed method is belonging. Typical DBT methods include single-frame detection approaches depending on image filtering, human visual system (HVS), pattern recognition and low-rank recovery theory.

To relaxed the sensitivity of traditional filtering methods to heavy noise or strong clutters, some filtering methods based on background content guidance are proposed such as edge directional TDLMS [12], new Tophat filter [29]. Unlike the above filtering methods, some methods attempt to find suspicious target region by delineating the local contrast of central area and its neighboring ones inspired by HVS. Chen et al. [14] put forward to use local contrast measure (LCM) to pop out the small target and suppress background clutters. Following this clue, an improved LCM (ILCM) built on subblocks of infrared image was designed in Reference [30]. Furthermore, several saliency detection schemes guided by multiple successive stages have been proposed for improving the detection accuracy. For instance, Qin and Li [15] proposed a novel LCM by employing difference of Gaussian filter and novel local saliency measure to suppress pixel-sized noises with high brightness. Yao *et al.* [31] suggested a coarse-to-fine detection system combing structured background recovery and unstructured clutter suppression. Wei *et al.* [32] provided a multiscale patch-based contrast measure (MPCM) to increase target contrast. Different from the methods that calculate local contrast using raw pixel values, some current methods integrate multiple features (e.g. information entropy, scale, direction, spatial distribution and variance-level features) to deal with the deficiency of single feature in gray level, such as method based on flux density jointing direction diversity [10], multiscale gray and variance difference measures (MGVD) [16], derivative entropy-based contrast measure (DECM) [19].

The small target detection task is usually regarded as a classification problem in pattern recognition-based methods, such as random walker [33], [34], convolutional neural network [35]. These methods are workable in scenarios covered by training feature samples or labels that include various small targets and clutters. However, practical long-range infrared scenes are so intricate that the limited training features hardly represent all the types of target and background [7]. Then, their performance might degrade rapidly.

In recent years, RPCA theory has been widely applied in target/object detection or segmentation task and achieves great success [22], [36], [37]. However, infrared small target detection is different from general object detection and separation tasks due to the unique characteristics of infrared small targets and complex backgrounds. In the seminal work of Gao *et al.* [9], the infrared small target detection task is inverted into RPCA problem with the help of IPI model. To ameliorate the performance of initial IPI model on infrared small target detection, then a series of improved schemes were developed one after another. Dai *et al.* [38] adopted target likelihood parameter computed by steering kernel as adaptive weight for the better suppression of clutters. In another effort [39], a total variation regularization was introduced to smooth the crisp edge in background. Zhang *et al.* [40] used the l_p-norm to constrain the target patch-image. In methods [41], [42], different nonconvex low-rank regularizers were used to constrain the background patch-image to get more accurate background estimation. In recent work [4], the IPI model was generalized to a novel infrared patch-tensor model (IPT) to dig more information from background patch-image. Zhang and Peng [43] and Sun *et al.* [44] exploited different optimization methods of tensor nuclear norm to improve the limitations of initial IPT. To improve the robustness of IPI model, some methods based on multi-subspace structure were designed, such as low-rank and sparse representation (LRSR) [45], stable multi-subspace learning methods (SMSL) [46]. Compared with the above low-rank recovery-based methods, our proposed method takes three considerations into account, namely accurate background recovery, adaptive sparse penalty parameter and preservation of inherent structure of background. Experiments demonstrate that our proposed method has better robustness and effectiveness, and achieves outperforming detection performance in comparison with the state-of-the-art methods.

III. GRAPH-REGULARIZED LAPLACE LOW-RANK APPROXIMATION MODEL (GRLA)

A. LAPLACE LOW-RANK REGULARIZER

Recently, some nonconvex low-rank approximation regularizers have achieved expressive performance in infrared small

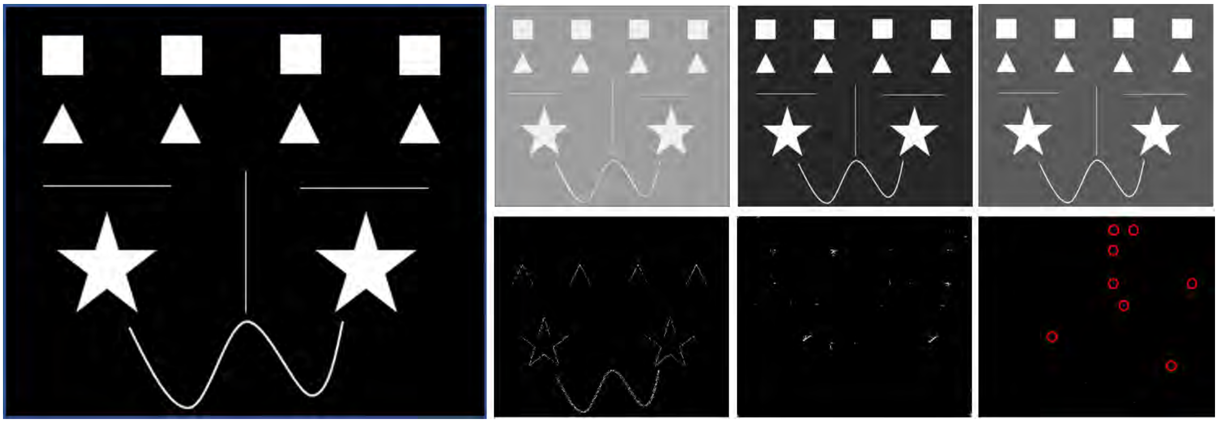

FIGURE 2. **Illustration of background recovery under different rank relaxations. The first row shows the recovered background and the second row presents the background residues. Column 1: Synthetic image. Column 2: Recovering result using nuclear norm. Column 3: Recovering result using $S_{1/2}$ norm. Column 4: Recovering result using Laplace norm. Red circles mark some salient points.**

detection field [41], [42]. Different from the non-convex low-rank constraint already used in small target detection frameworks, Laplace norm [47] as rank relaxation is used in the proposed model, which is defined as:

$$rank(\mathbf{L}) \approx ||\mathbf{L}||_{\gamma} = \sum_{i=1}^{\min\{m,n\}} (1 - e^{-\sigma_i(\mathbf{L})/\gamma}) \tag{2}$$

where $\gamma(\gamma > 0)$ is an approximation factor, controlling the degree of approximation to the original rank. It is a pseudo norm and its nice properties have been given in Ref. [47], which also play important role in our proposed model.

To illustrate the advantages of Laplace norm induced low-rank approximation, we will test some nonconvex matrix rank relaxations on a synthetic data. Fig. 2 shows the recovering results of a synthetic image using three rank relaxations: nuclear norm, Schatten 1/2-norm ($S_{1/2}$-norm) and Laplace norm. We set up various geometric structures in synthetic images, such as squares, triangles, pentagons, lines and curves. Their sparse edges and corners pose great challenges to background restoration. The second to fourth columns of Fig. 2 present the background recovering effect of different rank relaxations on synthetic image. As shown in the second column of Fig. 2, it is easily observed that many sparse edges are not fully recovered due to the limitation of nuclear-norm relaxation. The third column of Fig. 2 shows the result of background recovery using $S_{1/2}$-norm relaxation. We see that there are no edges but still exist substantial salient corners that are not recovered. The fourth column of Fig. 2 displays the result of Laplace norm approximation. It is seen that the restoration is better than others. There is almost no significant background residue.

B. NONNEGATIVE CONSTRAINT REWEIGHTED L_1-NORM FOR ENHANCING SPARSITY

As shown in the fourth column of Fig. 2, some weak corner point of geometries are still not recovered completely, which are marked by red circles. Intuitively, these points have similar intensity to the infrared dim target. Considering the drawbacks of l_1-norm as the sparsity measure of target patch-image, it would lead to a dilemma that the dim targets may be over-shrank resulting in high missing alarm or the nontarget points remain in the target image rising false alarm [38]. Therefore, it is necessary to use an adaptive shrinkage threshold to distinguish dim small target from background residues. Moreover, the key prior information that small target is usually more salient than its neighborhood should not be ignored. Hence, the negative values generated by matrix decomposition are unrelated to the target gray values. Adding a non-negative constraint to the target sparse measure will better fit the property of the target local saliency. Combining the reweighted view [48] and non-negative constraint, the sparse constraint term of the target patch-image is defined as the reciprocal form of gray value as following:

$$||\mathbf{W_S} \odot \mathbf{S}||_1 = \sum_{i,j} w_{i,j} s_{i,j} \tag{3}$$

where $\mathbf{W_S} = \{\mathbf{W_S}(i,j)\}$ are adaptive weights for the elements $\mathbf{S}_{i,j}$ of $\mathbf{S}$, which is described as:

$$\mathbf{W}_{\mathbf{S}}^{k+1}(i,j) = \begin{cases} \dfrac{1}{\mathbf{S}_{i,j}^{k} + \epsilon} & if\ \mathbf{S}_{i,j}^{k} \geq 0 \\ 0 & if\ \mathbf{S}_{i,j}^{k} < 0 \end{cases} \tag{4}$$

where ϵ is a smoothing parameter to avoid division zero.

C. THE CONSTRUCTION OF GRAPH REGULARIZATION

As above mentioned, the background patch-image has low-rank property owing to the nonlocal correlation in infrared background. However, the intrinsic local geometric structure of infrared background is destroyed in the construction of patch-image. Therefore, how to effectively explore and preserve the local structure of background patch-image will be of great significance. Inspired by Reference [26], a nearest neighbor graph is constructed to model and maintain the local structural information. The construction process of graph regularization is as follows.

Let $\mathbf{D} = [d_1, d_2, \ldots, d_P] \in \mathbb{R}^{D \times P}$ be the constructed infrared patch-image, in which P denotes the number of

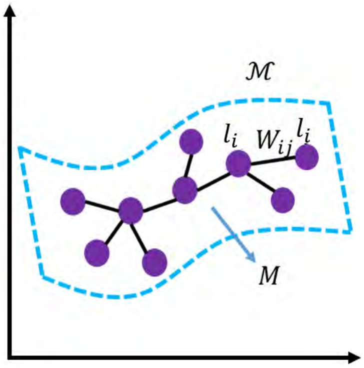

FIGURE 3. Graph construction on infrared patch-image.

patch image and each d_i $(i = 1, 2, \ldots, P)$ represents the ith vectorized image patch. $\mathbf{L} = [l_1, l_2, \ldots, l_P] \in \mathbb{R}^{D \times P}$ is the low-rank part representing the background patch-image. l_i $(i = 1, 2, \ldots, P)$ denotes the low-rank component of the ith background patch. To preserve the intrinsic geometrical structural in background patch-image, one may naturally hope that if two patches d_i and d_j are close in the intrinsic manifold, their corresponding low-rank components l_i and l_j are also close or similar too. Following this, a nearest neighbor graph $\mathbf{G}$ can be constructed by viewing each d_i as its vertex. The weighted matrix of $\mathbf{G}$ is denoted as $\mathbf{W}$. If d_i is one of the k-nearest neighbors of d_j, the weight is defined as:

$$W_{ij} = e^{-\frac{\|d_i - d_j\|_2^2}{\sigma_w^2}} \tag{5}$$

which is known as the heat kernel [49]. W_{ij} is the (i, j)th element of $\mathbf{W}$, and σ_w^2 is the variance of original patch-image. Recall that the corresponding low-rank components of any two background patches d_i and d_j are expected to maintain the same local structure among them. To achieve this, a reasonable way is to minimize the following function [49]:

$$\begin{aligned}
\frac{1}{2}\sum_{i,j=1}^{P} \|l_i - l_j\|_2^2 W_{ij} &= \frac{1}{2}\sum_{i,j=1}^{P} (l_i^T l_i + l_i^T l_i - 2 l_i l_j) W_{ij} \\
&= \frac{1}{2}(2\sum_{i=1}^{P} l_i^T l_i H_{ii} - 2\sum_{i=1}^{P} l_i^T l_i W_{ij}) \\
&= tr(\mathbf{LHL^T}) - tr(\mathbf{LWL^T}) \\
&= tr(\mathbf{LML^T})
\end{aligned} \tag{6}$$

where tr is the trace of a matrix, $\mathbf{H}$ is a diagonal matrix in which $H_{ii} = \sum_{j=1}^{P} W_{ij}$, and $\mathbf{M} = \mathbf{H}\text{-}\mathbf{W}$ is the graph Laplacian matrix. For a more intuitive observation, Fig. 3 shows the construction of a graph on an infrared patch-image.

Taking the three parts into consideration, we develop GRLA model for detecting small infrared target, which is formulated as:

$$\begin{aligned}
&\min_{\mathbf{L},\mathbf{S}} \|\mathbf{L}\|_\gamma + \lambda_1 \|\mathbf{W_S} \odot \mathbf{S}\|_1 + \lambda_2 tr(\mathbf{LML^T}) \\
&s.t.\ \ \mathbf{D} = \mathbf{L}+\mathbf{S}
\end{aligned} \tag{7}$$

where λ_1 and λ_2 represent the tradeoff between the sparse constraint and graph regularization.

IV. OPTIMIZATION PROCEDURE OF GRLA MODEL

A. OPTIMIZATION PROCEDURE

In this section, we present how to solve GRLA model by Alternating Direction Method of Multipliers (ADMM) [27]. The problem (7) is first converted to the equivalent type.

$$\begin{aligned}
&\min_{\mathbf{L},\mathbf{S}} \|\mathbf{L}\|_\gamma + \lambda_1 \|\mathbf{W_S} \odot \mathbf{S}\|_1 + \lambda_2 tr(\mathbf{ZMZ^T}) \\
&s.t.\ \ \mathbf{D} = \mathbf{L}+\mathbf{S}, \quad \mathbf{L} = \mathbf{Z}
\end{aligned} \tag{8}$$

Subsequently, the problem (8) is transformed as minimizing the following augmented Lagrange function:

$$\begin{aligned}
\mathcal{L} = &\|\mathbf{L}\|_\gamma + \lambda_1 \|\mathbf{W_S} \odot \mathbf{S}\|_1 + \lambda_2 tr(\mathbf{ZMZ^T}) \\
&+ \langle \mathbf{Y}_1, \mathbf{D} - \mathbf{L} - \mathbf{S} \rangle + \langle \mathbf{Y}_2, \mathbf{Z} - \mathbf{L} \rangle \\
&+ \frac{\mu_1}{2}\|\mathbf{D} - \mathbf{L} - \mathbf{S}\|_F^2 + \frac{\mu_2}{2}\|\mathbf{Z} - \mathbf{L}\|_F^2
\end{aligned} \tag{9}$$

where μ_1 and μ_2 are positive penalty parameters, $\mathbf{Y}_1$ and $\mathbf{Y}_2$ are the Lagrangian multiplier, and $\langle \cdot, \cdot \rangle$ stands for the standard trace inner product, i.e $\langle \mathbf{A}, \mathbf{B} \rangle = trace(\mathbf{A}^T\mathbf{B})$. The minimization of the problem (9) can be iteratively solved by alternatively updating every variable in the augmented Lagrange function while fixing others. In the following, we give the details for each iteration.

Updating $\mathbf{L}$ when fixing the latest values of other variables.

$$\begin{aligned}
\mathbf{L}^{k+1} &= \arg\min_{\mathbf{L}} \mathcal{L}(\mathbf{L}, \mathbf{S}^k, \mathbf{Z}^k, \mathbf{Y}_1^k, \mathbf{Y}_2^k, \mu_1^k, \mu_2^k) \\
&= \arg\min_{\mathbf{L}} \|\mathbf{L}\|_\gamma + \left\langle \mathbf{Y}_1^k, \mathbf{D} - \mathbf{L} - \mathbf{S}^k \right\rangle + \left\langle \mathbf{Y}_2^k, \mathbf{Z}^k - \mathbf{L} \right\rangle \\
&\quad + \frac{\mu_1^k}{2}\|\mathbf{D} - \mathbf{L} - \mathbf{S}^k\|_F^2 + \frac{\mu_2^k}{2}\|\mathbf{Z}^k - \mathbf{L}\|_F^2 \\
&= \arg\min_{\mathbf{L}} \tau \|\mathbf{L}\|_\gamma + \frac{1}{2}\|\mathbf{L} - \mathbf{X}_{\mathbf{L}}^k\|_F^2
\end{aligned} \tag{10}$$

where $\mathbf{X}_{\mathbf{L}}^k = (\mu_1^k(\mathbf{D} - \mathbf{S}^k + \mathbf{Y}_1^k/\mu_1^k) + \mu_2^k(\mathbf{Z}^k + \mathbf{Y}_2^k/\mu_2^k))/(\mu_1^k + \mu_2^k)$. Due to the nonconvex property of Laplace-norm, the conventional singular values threshold (SVT) [50] algorithm fails in the subproblem (10). Fortunately, as demonstrated in [51], the approximate solution of the subproblem (10) can be obtained by the generalized weight singular value threshold (WSVT) operator. The detailed procedure of the subproblem (10) using WSVT is shown in **Algorithm 1**.

Updating $\mathbf{S}$ when fixing the latest values of other variables.

$$\begin{aligned}
\mathbf{S}^{k+1} &= \arg\min_{\mathbf{S}} \mathcal{L}(\mathbf{L}^{k+1}, \mathbf{S}, \mathbf{Z}^k, \mathbf{Y}_1^k, \mathbf{Y}_2^k, \mu_1^k, \mu_2^k) \\
&= \arg\min_{\mathbf{S}} \lambda_1 \|\mathbf{W}_\mathbf{S}^k \odot \mathbf{S}\| + \left\langle \mathbf{Y}_1^k, \mathbf{D} - \mathbf{L}^{k+1} - \mathbf{S} \right\rangle \\
&\quad + \frac{\mu_1^k}{2}\|\mathbf{D} - \mathbf{L}^{k+1} - \mathbf{S}\|_F^2 \\
&= \arg\min_{\mathbf{S}} \frac{\lambda_1}{\mu_1^k}\|\mathbf{W}_\mathbf{S}^k \odot \mathbf{S}\| + \frac{1}{2}\|\mathbf{S} - \mathbf{X}_\mathbf{s}^k\|_F^2
\end{aligned} \tag{11}$$

Algorithm 1: Solving Laplace-Norm Minimization

```
Input: $\mathbf{L}^k, \gamma, \tau, \mathbf{X}_\mathbf{L}^k, \Lambda^0$;
Initialize: $t = 0$, $[\mathbf{U}\ \Sigma_{ii}\ \mathbf{V}] = svd(\mathbf{X}_\mathbf{L}^k)$;
For convenience, define $\varphi_i(\sigma_i^k) = 1 - e^{-\sigma_i^k(\mathbf{L})/\gamma}$ and
$\partial\varphi_i(\sigma_i^k)$ is the derivative of $\varphi_i(\sigma_i^k)$ with respect to $\sigma_i^k$.
while not converged do
    1: Solving $\Sigma^{t+1}$
    $\partial\varphi_i(\sigma_i^k) = \frac{1}{\gamma}e^{-\sigma_i^k(\mathbf{L})/\gamma}$,
    $\Sigma_{ii}^{t+1} = \max(\Sigma_{ii} - (\partial\varphi_i(\sigma_i^k)/\gamma))$
    2: Convergence condition
    $||\Sigma^{t+1} - \Sigma^t||_F < \varepsilon$
end
Output: $\mathbf{L}^{k+1} = [\mathbf{U}\ \Sigma^{t+1}\ \mathbf{V}]$;
```

where $\mathbf{X}_\mathbf{s}^k = \mathbf{D} - \mathbf{L}^{k+1} + \mathbf{Y}_1^k/\mu_1^k$. The above problem is solved by the conventional soft threshold operator [50].

$$\mathbf{S}^{k+1} = \mathbf{S}_{\frac{\lambda_1}{\mu_1^k}\mathbf{W}_\mathbf{s}^k}(X_\mathbf{S}^k) \tag{12}$$

Updating $\mathbf{Z}$ when fixing the latest values of other variables.

$$\begin{aligned}\mathbf{Z}^{k+1} &= \arg\min_{\mathbf{Z}} \mathcal{L}(\mathbf{L}^{k+1}, \mathbf{S}^{k+1}, \mathbf{Z}, \mathbf{Y}_1^k, \mathbf{Y}_2^k, \mu_2^k)\\ &= \arg\min_{\mathbf{Z}} \lambda_2 tr(\mathbf{Z}\mathbf{M}\mathbf{Z}^T) + \left\langle \mathbf{Y}_2^k, \mathbf{Z} - \mathbf{L}^{k+1}\right\rangle\\ &\quad + \frac{\mu_2^k}{2}||\mathbf{Z} - \mathbf{L}^{k+1}||_F^2\end{aligned} \tag{13}$$

The solution of the Eq. (13) is obtained by setting the derivative of the equation with respect to $\mathbf{Z}$ to zero.

$$\mathbf{Z}^{k+1} = (2\frac{\lambda_2}{\mu_2^k}\mathbf{M} + \mathbf{I})^{-1}(\mathbf{L}^{k+1} - \mathbf{Y}_2^k/\mu_2^k) \tag{14}$$

Updating $\mathbf{Y}_1$, $\mathbf{Y}_2$, μ_1, μ_2 when fixing the latest values of other variables. For convenience and without loss of generality, we initially set $\mu_1^0 = \mu_2^0 = \mu^0$.

$$\mathbf{Y}_1^{k+1} = \mathbf{Y}_1^k + \mu^k(\mathbf{D} - \mathbf{L}^{k+1} - \mathbf{S}^{k+1}) \tag{15}$$

$$\mathbf{Y}_2^{k+1} = \mathbf{Y}_2^k + \mu^k(\mathbf{Z}^{k+1} - \mathbf{L}^{k+1}) \tag{16}$$

The optimization procedure of the proposed model is outlined in **Algorithm 2**.

Algorithm 2: GRLA Model for Detecting Small Infrared Target

```
Input: Infrared Patch-image $\mathbf{D}$, $\gamma$, $\lambda_1$, $\lambda_2$;
Initialize: $\mathbf{L}^0 = \mathbf{S}^0 = \mathbf{Z}^0 = 0$; $\mathbf{Y}_1^0 = \mathbf{Y}_2^0 = 0$; $\mu^0 = \frac{1.25}{||\mathbf{D}||^2}$; $\mu_{\max} = 10^7$; $\varepsilon = 10^{-7}$; $k = 0$; $\rho = 1.1$;
while not converged do
    Solving $\mathbf{L}^{k+1}$ by Algorithm 1.
    Solving $\mathbf{S}^{k+1}$ by (12).
    Solving $\mathbf{Z}^{k+1}$ by (14).
    Solving $\mathbf{Y}_1^{k+1}$ by (15).
    Solving $\mathbf{Y}_2^{k+1}$ by (16).
    Updating $\mathbf{W}_\mathbf{S}^{k+1}$ by (4)
    Updating $\mu^{k+1} = \min(\rho\mu^k, \mu_{\max})$
    Check the convergence condition
    $\frac{||\mathbf{D}-\mathbf{L}^{k+1}-\mathbf{S}^{k+1}||_F}{||\mathbf{D}||_F} < \varepsilon$ or $||\mathbf{S}^{k+1}||_0 = ||\mathbf{S}^k||_0$
    $k = k + 1$
end
Output: $\mathbf{L}$ and $\mathbf{S}$;
```

B. GENERALIZE THE MODEL TO OTHER NON-CONVEX LOW-RANK APPROXIMATION CASE

Recently, many researchers have concentrated on how to achieve better low-rank recovery by developing different nonconvex norm instead of nuclear norm [47], [52]. Here, we extend our model into a generalized nonconvex model with the help of different nonconvex rank functions, named as Generalized Graph-regularized nonconvex low-rank approximation model (G-GRLA). The generalized model can be described as:

$$\begin{aligned}&\min_{\mathbf{L},\mathbf{S}} ||\mathbf{L}||_{NC-Norm} + \lambda_1||\mathbf{W_S} \odot \mathbf{S}||_1 + \lambda_2 tr(\mathbf{Z}\mathbf{M}\mathbf{Z}^\mathbf{T})\\ &s.t.\ \ \mathbf{D} = \mathbf{L} + \mathbf{S},\ \ \mathbf{L} = \mathbf{Z}\end{aligned} \tag{17}$$

where $||\mathbf{L}||_{NC-Norm}$ represents different nonconvex rank functions.

ADMM [27] is still used to optimize the model. With other equations unchanged, we only convert (10) to the following problem:

$$\begin{aligned}\mathbf{L}^{k+1} &= \arg\min_{\mathbf{L}} \mathcal{L}(\mathbf{L}, \mathbf{S}^k, \mathbf{Z}^k, \mathbf{Y}_1^k, \mathbf{Y}_2^k, \mu_1^k, \mu_2^k)\\ &= \arg\min_{\mathbf{L}} \tau||\mathbf{L}||_{NC-Norm} + \frac{1}{2}||\mathbf{L} - \mathbf{X_L}||_F^2\end{aligned} \tag{18}$$

Now we provide several possible examples as following: For weighted S_p-norm, the problem (18) is effectively solved using generalized soft-threshold (GST) [52]; For $S_{1/2}$-norm, we employ the half-threshold operator [53] to solve the problem; For arctangent rank function [54] and γ-norm [55], they are optimized by difference of convex (DC) programming [56]. As soon as obtaining $\mathbf{L}^{k+1}$, the other variables $\mathbf{S}^{k+1}$, $\mathbf{Z}^{k+1}$, $\mathbf{Y}_1^{k+1}$ and $\mathbf{Y}_2^{k+1}$ are alternately solved by (12), (14), (15) and (16) separately.

C. DETECTION PROCEDURE

In Fig. 4, we provide the whole schematic of GRLA model for detecting small target. The detailed steps are as follows:

1) Constructing the infrared patch-image $\mathbf{D}$ via the same patch-image construction as the IPI model.

2) **Algorithm 2** is exploited to implement the target-background separation.

3) According to the uniform average of estimators (UAE) reprojection scheme, the background image f_L and target image f_S can be reconstructed from the background patch-image $\mathbf{L}$ and target patch-image $\mathbf{S}$.

4) The final target is separated by an adaptive threshold, which is determined by:

$$T_{up} = \max(\upsilon_{\min}, \beta + k\sigma) \tag{19}$$

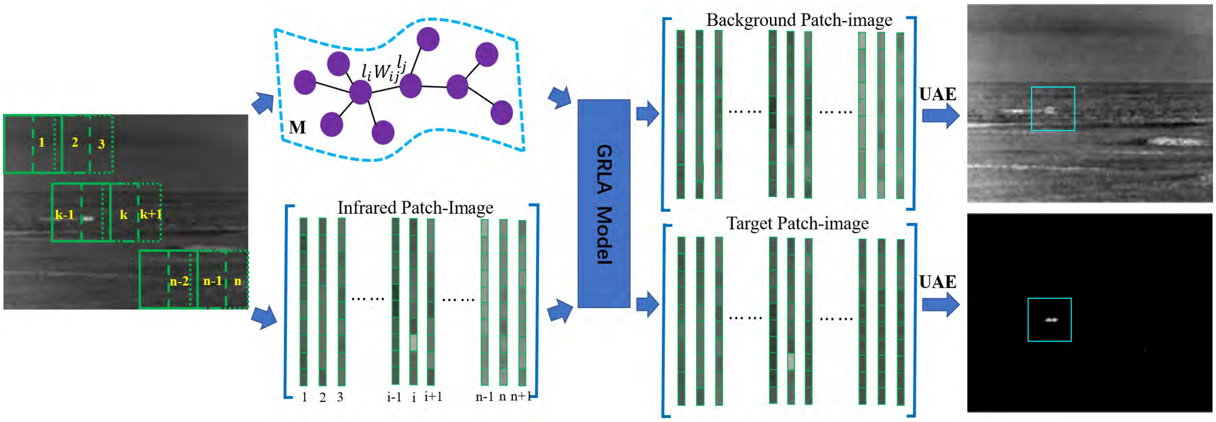

FIGURE 4. **The Schematic of GRLA model for detecting small target.**

where β and σ are the mean value and standard deviation of the target image f_E, respectively. k and $\upsilon_{\min}$ are constants determined experientially.

V. EXPERIMENTAL ANALYSIS

In order to fully validate the proposed model, we conduct experiments on extensive actual infrared scenes involving different complex background and compare twelve state-of-the-art methods in terms of subjective visual and objective evaluation.

A. EVALUATION CRITERIONS

Several frequently used criterions are introduced to quantitatively evaluate the performance of all tested algorithms for comparison.

The probability of detection (P_d) and the false alarm rate (F_a) are the vital metrics to quantify the performance of the detection methods. They are defined as

$$P_d = \frac{number\ of\ true\ detections}{number\ of\ actual\ targets} \tag{20}$$

$$F_a = \frac{number\ of\ false\ detections}{number\ of\ images} \tag{21}$$

A good detector should possess high P_d while having low F_a at the same time. The receiver operating characteristic (ROC) plots the tradeoff between P_d and F_a. Here, we assume that the detected results are correct in the case when there is positive pixel in the 5×5 window centered on the ground truth.

Signal-to-clutter ratio (SCR) is widely used as a descriptor of the target saliency, denoting the degree of difficulty in detection and defining as:

$$SCR = \frac{|\mu_t - \mu_b|}{\sigma_b} \tag{22}$$

where μ_t and μ_b are the average grayscale of the target area and its surrounding region, respectively. σ_b stands for standard deviation of the neighborhood region. SCR-gain (SCR_G) represents the enhancement of target saliency before and after processing. It is defined as:

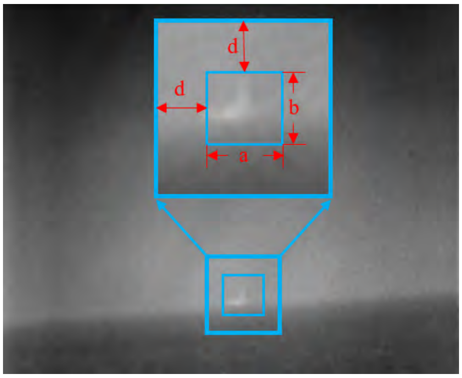

FIGURE 5. **Infrared small target and local background region in infrared image.**

$$SCR_G = \frac{SCR_{out}}{SCR_{in}} \tag{23}$$

where SCR_{in} and SCR_{out} are the SCR values before and after target detection separately. Background suppression factor (BSF) presents the background suppression ability of detection methods, which is formulated as:

$$BSF = \frac{\sigma_{in}}{\sigma_{out}} \tag{24}$$

where σ_{in} and σ_{out} are the standard deviation of background neighborhood in original image and the suppressed image. The higher the SCR_G and BSF values are, the superior the performance of target enhancement and background suppression is. They are calculated in a local region, as presented in Fig. 5. Suppose the target region is $a \times b$, and $d = 20$ is the neighborhood width.

B. BASELINE METHODS AND TEST DATASETS

Baseline Methods: Twelve state-of-the-art approaches are involved in the experiments as baseline methods. Among them, Max-Median [11] and Tophat [13] are filtering methods. ILCM [30], MPCM [32], WLDM [17] and LSM [18]

TABLE 1. Summary of all tested methods and their detailed parameter settings.

Assumption	Methods	Parameter settings
Background consistency	Max-Median [11]	support size:5×5
	Tophat [13]	structure shape: square, structure size 3×3
Target saliency	ILCM [30]	subblock size: 8×8, moving step: 4, $k \in [1, 2]$
	MPCM [32]	$N = 1, 3, ..., 9$
	WLDM [17]	$L = 4$,$m = 2$,$n = 2$
	LSM [18]	$a \in [2, 4]$, $g = 0.6$
Nonlocal correlation of background and sparsity of target	IPI [9]	patch size: 50×50,sliding size: 10, λ=$L/min(m, n)^{1/2}$, $L \in [1, 5]$, ε= 10^{-7}
	NIPPS [41]	patch size: 50×50, sliding size: 10, λ=$L/min(m, n)^{1/2}$, $L \in [1, 5]$, energy constraint ratio: $r \in [0.01, 0.05]$
	RIPT [4]	patch size: 50×50 or 30×30, sliding size: 10, λ=$L/min(I,J,P)^{1/2}$, $L \in [0.5, 2]$,$h = 10$,ϵ=0.01, ε= 10^{-7}
	TV-PCP [39]	patch size: 50×50, sliding size: 12,$\lambda 2$=$L/min(m, n)^{1/2}$, $L \in [1, 5]$, $\lambda = 0.005$,β=0.025,$\gamma = 1.5$, ε= 10^{-7}
	SMSL [46]	patch size: 50×50, λ=$L/min(m, n)^{1/2}$, $L \in [3, 7]$
	NRAM [42]	patch size:50×50, sliding step:10, λ= $1/\sqrt{\min(m, n)}$, $\mu^0 = 3\sqrt{\min(m, n)}$,$\gamma = 0.002$, $C = \sqrt{\min(m, n)}/2.5$, $\varepsilon = 10^{-7}$
	GRLA	patch size: 30×30, sliding step: 12,$\lambda_1 = L/\sqrt{\max(m, n)}$, $L \in [4, 6]$, $\lambda_2 = G/\sqrt{\min(m, n)}$,$G \in [3, 5]$, $\gamma = 0.01$, $\epsilon = 0.01$,$\varepsilon = 10^{-7}$

are saliency-based methods. IPI [9], NIPPS [41], RIPT [4], TV-PCP [39], SMSL [46] and NLRA [42] belong to low-rank recovering methods. All tested methods and their parameter settings involved in the experiments are listed in Table 1. They are implemented using MATLAB 2018b on a PC with Intel Core i5 CPU 3.4 GHz and 8GB RAM.

Test Datasets: In order to verify the stableness of the proposed method to diverse scenes, extensive practical infrared images including single frames and sequences are tested. Considering that detecting weak small target from background with strong clutters is always a great challenge for existing detection methods, a superior detection performance for the extremely complex images carries more conviction than relatively simple images. Hence, 18 infrared images covering diverse target types and complex scenes are used to exhibit the performance of the proposed method in following experiments, as illustrated in Fig. 6. Their detailed information is listed in Table 2. All small targets are marked with cyan box and enlarged to facilitate weak target observation.

C. EVALUATION OF THE PROPOSED ALGORITHM

1) ROBUSTNESS TO DIFFERENT SCENES

In the Fig. 6, the 18 infrared images with various scenes have low spatial resolution/SCR values, noisy bright spot, heavy cloudy/sea clutters and bright man-made buildings. The size of small targets in these scenes varies greatly. For example, as displayed in Fig. 6(c, h, m-p), the number of pixels occupied by the target areas are less than 5 × 5, liking bright points in local background. The target containing in the scenes of Fig. 6(b, e, q, r) are larger than the previous ones, which possess the size range from 5 × 5 to 10 × 10. There are some targets beyond the defined ranges of infrared small target whose regions are greater than 10 × 10, as shown in Fig. 6(a, d, f, k, l). Moreover, the intensity of targets changes from extremely dim to very bright. The 3-D gray distribution of separated targets using the proposed method is given for intuitively observing, as shown in Fig. 7. Observing the Fig. 7, it can be found that the target and background are completely separated without any background components left in target images. Under these scenes, it is fair to conclude that the proposed method has good robustness for different complex background, target size and intensity.

2) COMPARISON WITH THE STATE-OF-THE-ART METHODS

Qualitative Comparisons: In this subsection, the ability of clutter suppression and target detection of the proposed model is demonstrated by compared with twelve state-of-the-art methods qualitatively. Fig. 8- 9 present the experimental results obtained by all tested methods on six single-frame images. For the results of Max-Median filter, the targets can be enhanced, but the strong edges and pixel-sized noise are also enhanced at the same time, as illustrated in Fig. 8(b1,c1),9(a1,c1). It can be seen in the results of TopHat operator that all targets are well detected. But there are some strong edge residues in the detection map owing to the usage of uncoordinated structural elements to depict the background, such as Fig. 8(a2-c2),9(a2,c2). Observing the results of ILCM, we can clearly see that ILCM highlights the targets while outstanding other bright non-target structures as well. In the results of MPCM, targets are enhanced remarkably and background clutters are suppressed very well. However, when confronting with the background with low signal-to-clutter ratio, some point-like nontarget with high brightness still remain in the final detection results, as illustrated in Fig. 8(b4,c4),9(a4-c4). For WLDM and LSM, there are some clutter residues in

TABLE 2. **Detailed information of all tested infrared images.**

Classification	Sequences	Numbers	Target Features	Background Features
Deep-space Background	Seq. 1-4	36/400	Irregular shape, brightness varying from extremely dim to bright close or on clutter edges	Comparatively smooth background clutter, backgrounds with heavy noise, artificial building near the targets
Sea-Clutter Background	Seq. 5	36/200	Target size varies greatly. Relatively high contrast to the surrounding background. appear on the sea-sky line	Background with strong ocean clutters and bright sea glint. Intensity varies greatly, island near the targets
Cloudy-Sky Background	Seq. 6	38/30	Small round-shape, very dim with relatively low contrast to the neighboring background some targets appear on cloudy edges	Various types of cloud clutters, such as cirrus, banded cloud and floccus. Diverse obvious man-made structure interference
Sky-Terrain Background		30	Target size and brightness changes greatly. Target with irregular shape.	Complex background scene with heavy clutter. Bright artificial buildings and plants disturbance.

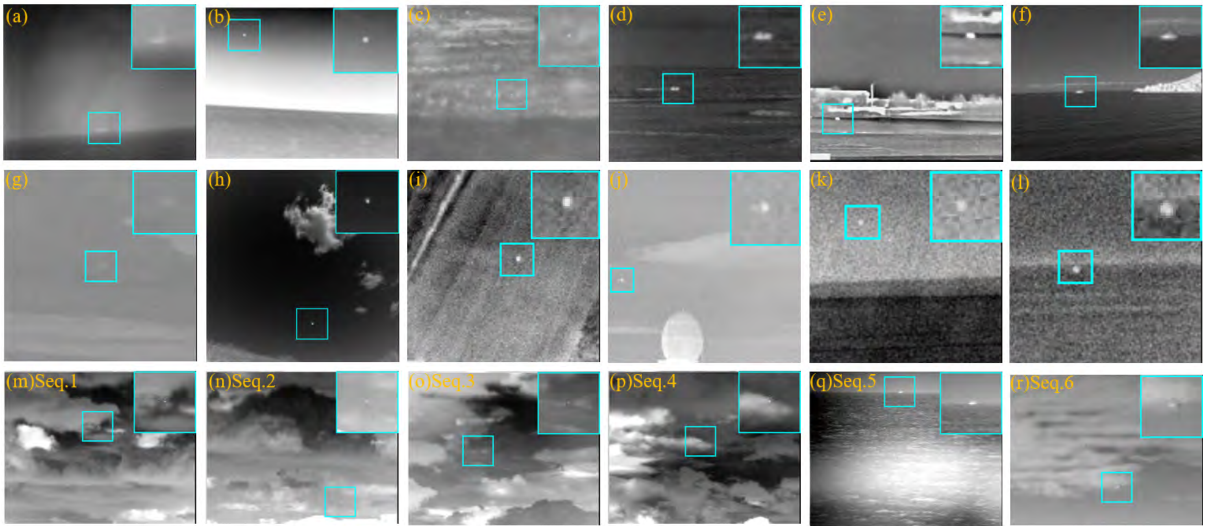

FIGURE 6. **The 18 real infrared images with diverse scenes. The labelled area is enlarged for better visualization.**

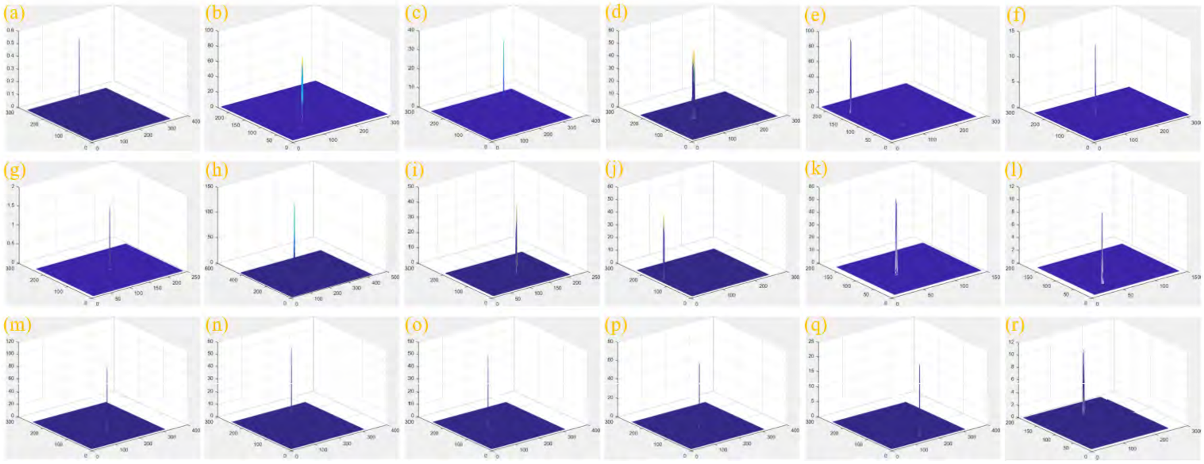

FIGURE 7. **For the 18 different complex scenes, (a)-(r) present the 3-D gray maps of separated targets using the proposed method.**

their result maps, as shown in Fig. 8(a5,c5),9(a5,c5). From the above observations, we can find that the filtering and saliency-based methods may be not stable enough for complex background.

The last six methods are all based on low-rank recovery. Compared with the above methods, they have better performance in background suppression. Specially, the result maps of the last six methods, as shown in rows 2, 4 and 6

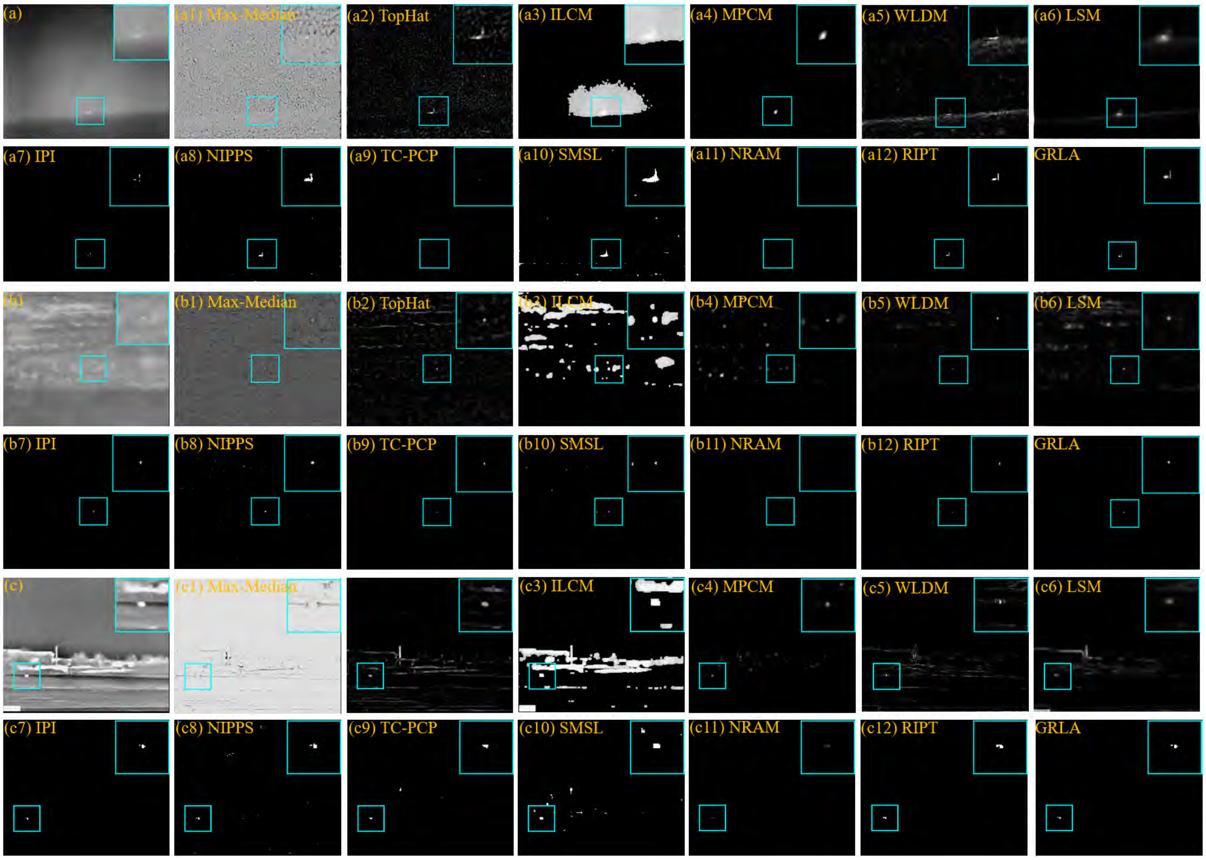

FIGURE 8. Detection results obtained by 12 compared methods. For better visualization, the demarcated region is enlarged in the right up corner.

of Fig. 8-9, have fewer clutter residuals. From the separated target images of IPI, we notice that the real targets are well detected, but some strong edges and bright spots are still retained, such as Fig. 9(a7,b7). There are several salient point false alarms in the results of NIPPS. From the results of SMSL, it easily finds that there is not only salient point but also clutters residuals, which shows that the subspace learning strategies may lack stability in these scenarios, especially those with spot-like components. Some outliers are left in the results obtained by TV-PCP, as shown in Fig. 8(c9). It may be that total variation regularization can smooth strong edges well but fail in pixel-sized points with high intensity. For the separated target images achieved by RIPT and NRAM, it is clearly that there are no non-target residues. However, the non-convex low-rank approximation within NRAM might lead to over-restoration of background, i.e. taking the target components as background, causing missing alarm (as shown in Fig. 8(a11,b11) or weakening targets (as shown in Fig. 9(a11-c11). The results of RIPT have several sparse nontarget points because they own similar sparsity to small target such as Fig. 9(a12,b12). Different from RIPT and NRAM, the sparse reweighted scheme, graph regularization and Laplace norm are integrated into the proposed model to overcome their drawbacks. The detection results obtained by our model have less clutter and noise residues under various complex backgrounds, as illustrated in Fig. 8- 9. Therefore, the proposed method has outperforming performance both in background suppression and target preservation among the 12 tested methods.

Quantitative Comparisons: Two objective indices SCR_G and BSF are used for evaluating the performance of the proposed method and comparison methods quantitatively. Table 3 gives the experimental data obtained by all tested methods on Fig. 8-9. For the two metrics, the higher values achieve, the better performance is. In this table, **Inf** is the abbreviation of infinite which indicates that the target surrounding area is completely shrink to zero, and '-' denotes that the target is undetected. Except for **Inf**, the first three optimal results are also highlighted with green, yellow and cyan blocks, respectively. In Table 3, it is clearly observed that the scores of our method are all **Inf** in terms of SCR_G and BSF. It indicates that the local background clutters are suppressed completely by our proposed method. The result is consistent with the segmentation result shown in Fig. 7. It shows that the proposed method achieves the best background suppression and target detection among 12 comparison methods.

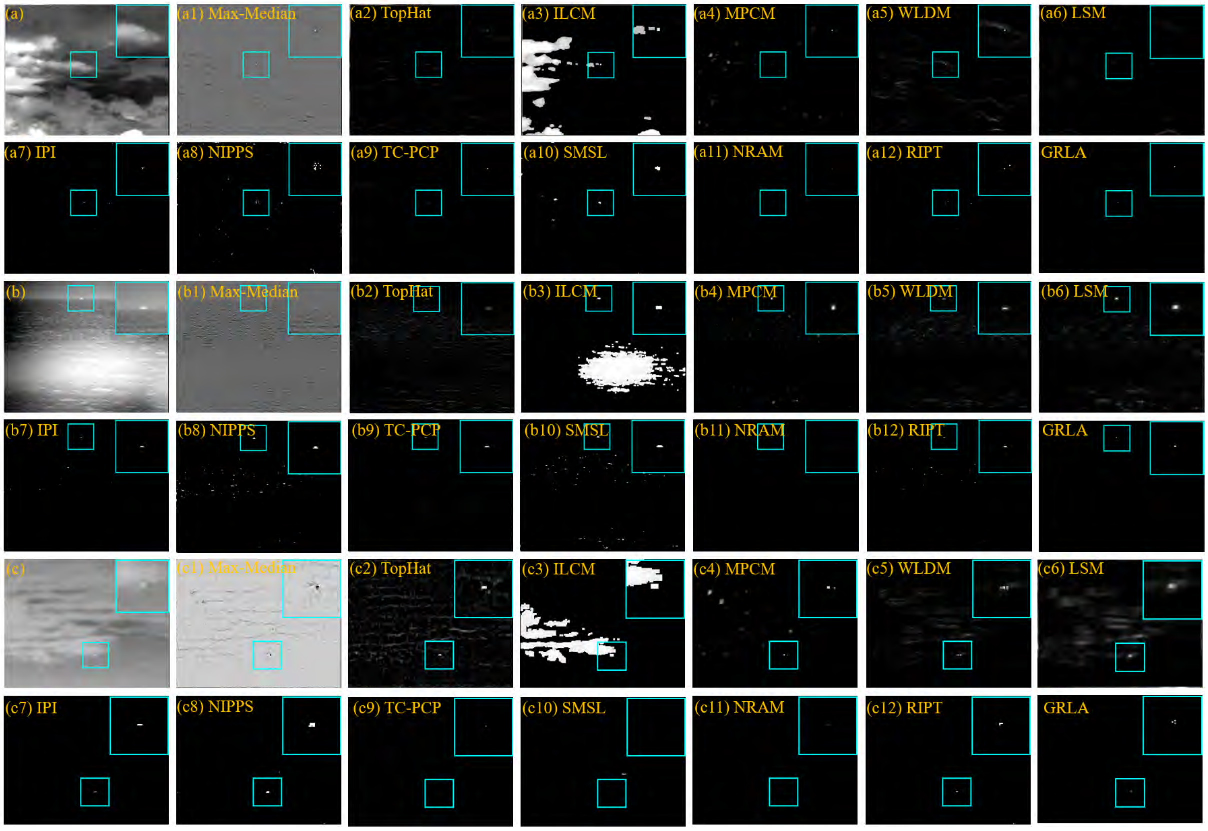

FIGURE 9. Detection results obtained by 12 compared methods. For better visualization, the demarcated region is enlarged in the right up corner.

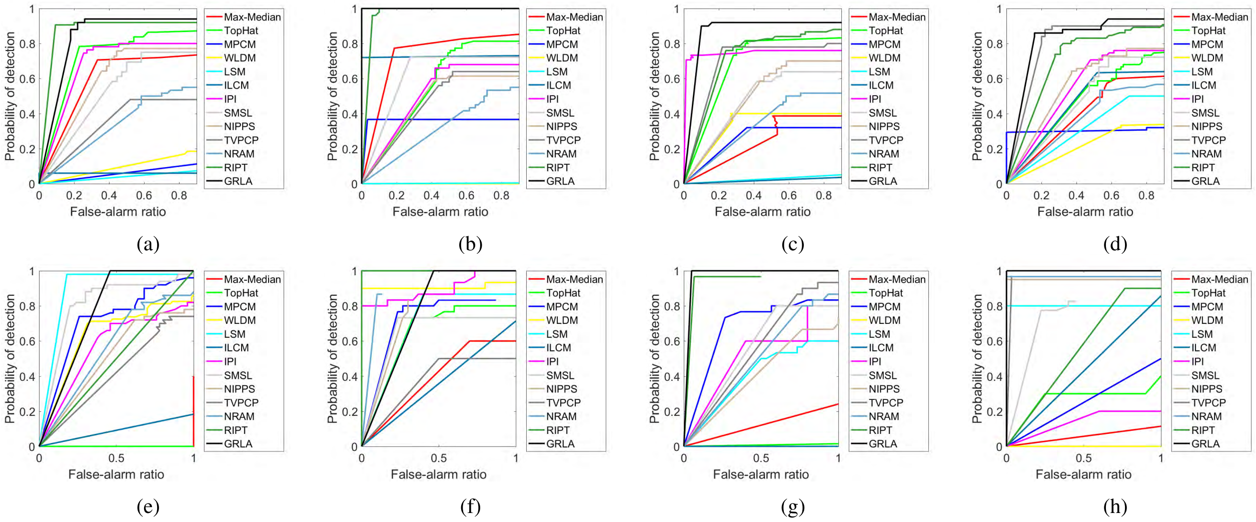

(a) (b) (c) (d)

(e) (f) (g) (h)

FIGURE 10. The ROC curves of detection results obtained using different methods (a) Sequence 1. (b) Sequence 2. (c) Sequence 3. (d) Sequence 4. (e) Sequence 5. (f) Sequence 6. (g) Group 1. (h) Group 2.

To verify the robustness of the proposed method, we give the ROC curves of all tested methods on six real infrared sequences, as illustrated in Fig. 10(a-f). In addition, the single-frame scenes are divided averagely into two groups according to the target size, that is, from 1 × 1 to 5 × 5 and from 5 × 5 to 10 × 10. Then, the ROC curves of each groups under all comparison methods are provided, as displayed in Fig. 10(g-h). It aims to estimate the stability of the proposed algorithm for different size targets in different scenarios. From the figures, we observe that the performance

TABLE 3. Detection performance comparison by two evaluation metrics in Fig. 8-9.

Methods	Evaluation Metrics	Fig.8(a)	Fig.8(b)	Fig.8(c)	Fig.9(a)	Fig.9(b)	Fig.9(c)
Max-Median	SCR_G	0.30	2.51	0.14	2.39	3.22	2.08
	BSF	21.77	4.75	5.72	20.16	16.44	6.52
TopHat	SCR_G	3.56	3.52	6.57	1.61	5.19	3.92
	BSF	18.74	4.51	9.91	9.28	10.32	6.26
ILCM	SCR_G	0.54	0.55	3.77	20.27	8.58	4.26
	BSF	21.52	18.20	25.82	40.10	16.46	14.36
MPCM	SCR_G	16.3562	12.6446	14..6488	72.63	48.66	75.51
	BSF	188.7708	155.9847	44.6101	291.69	177.36	220.98
WLDM	SCR_G	5.02	9.33	5.14	32.16	28.22	16.78
	BSF	33.50	28.50	52.13	111.99	60.18	40.52
LSM	SCR_G	7.08	2.82	2.76	-	130.76	30.35
	BSF	156.98	154.71	48.59	-	130.33	50.26
IPI	SCR_G	25.37	150.61	546.22	15569.86	23686.32	**Inf**
	BSF	813.94	97.11	227.12	4868.14	46561.16	**Inf**
NIPPS	SCR_G	15.63	56.45	37.64	156.71	102.14	**Inf**
	BSF	80.46	69.96	71.65	84.43	184.61	**Inf**
TV-PCP	SCR_G	371.93	53.91	49.65	**Inf**	**Inf**	**Inf**
	BSF	1658.08	157.11	171.69	**Inf**	**Inf**	**Inf**
SMSL	SCR_G	8.89	26.44	15.46	2248.68	192.13	-
	BSF		73.19	102.52	4698.81	386.42	-
NRAM	SCR_G	-	**Inf**	594.37	-	**Inf**	**Inf**
	BSF	-	**Inf**	2233.24	-	**Inf**	**Inf**
RIPT	SCR_G	**Inf**	**Inf**	**Inf**	17620.46	8234.53	**Inf**
	BSF	**Inf**	**Inf**	**Inf**	31896.45	12784.06	**Inf**
GRLA	SCR_G	**Inf**	**Inf**	**Inf**	**Inf**	**Inf**	**Inf**
	BSF	**Inf**	**Inf**	**Inf**	**Inf**	**Inf**	**Inf**

[1] In the low-rank based methods, 'Inf' merely means that the target neighborhood is completely suppressed, which is marked in red. '-' denotes that there is no target in the final detected result. Except for 'Inf' and '-', the best three results are highlighted with green, yellow and cyan separately.

TABLE 4. Average P_d and F_a obtained by proposed method.

Synthetic Images	Indexes	Original	# 1	# 2	# 3	# 4
NA-Group (/image)	P_d	1	0.93	0.80	0.68	0.41
	F_a	0.5	1.2	2.8	3.9	7.6
NR-Group (/image)	P_d	1	1	0.95	0.93	0.93
	F_a	0.5	0.7	0.7	1.4	2.2

of different tested algorithms varies greatly in sequences and single-frames groups. But our proposed method achieves the best performance for different backgrounds as compared with baseline methods. It is noteworthy that P_d values of our proposed method are less than TV-PCP in Sequence 4 and RIPT in Sequence 6 when F_a is less than 0.5. However, when the false alarm is greater than 0.5, the detection of probability of the proposed algorithm will be greater than that of the two compared methods, and even reach 100% detection rate. The saliency-based methods obtain unsatisfactory detection performance in Sequences 1-4 and two single-frame groups. Observing the Fig. 10(g-h), it is clearly that the methods based on low-rank recovery are more stable than other methods in single-frame scenarios with different size targets. Among them, our algorithm performs more robust than the comparison methods. In conclusion, the ROC curves of all tested results show that the proposed method have obvious advantages in the robustness and effectiveness of target detection compared with all experimental methods.

3) ROBUSTNESS TO NOISY SCENES

Except for the complex and changeable imaging background, small infrared targets will be contaminated by various noise derived from sensor and natural factors. It would result in reducing the brightness and contrast of the target and declining the accuracy of detection. Here, two schemes are designed to evaluate performance of the proposed method with respect to different level noise. On one hand, white Gaussian noise is added to 6 complex scenes that are selected from Fig. 7. Then, different level noise is added to the selected images. The proposed method is used to test the noisy images. When the noise standard deviation is 10, the target detection and background suppression could be well achieved (Fig. 11(g-l)). As the noise standard variance increases to 20, the proposed method still locates the target exactly in Fig. 11(m,n,o,r), but fails in Fig. 11(p). Nevertheless, the result is still acceptable because the small target in Fig. 11(p) has been completely submerged in the noise.

On the other hand, Monte-Carlo study is used to analyze the noise influence for the proposed method with plenty of white Gaussian noise realizations for each noise level.

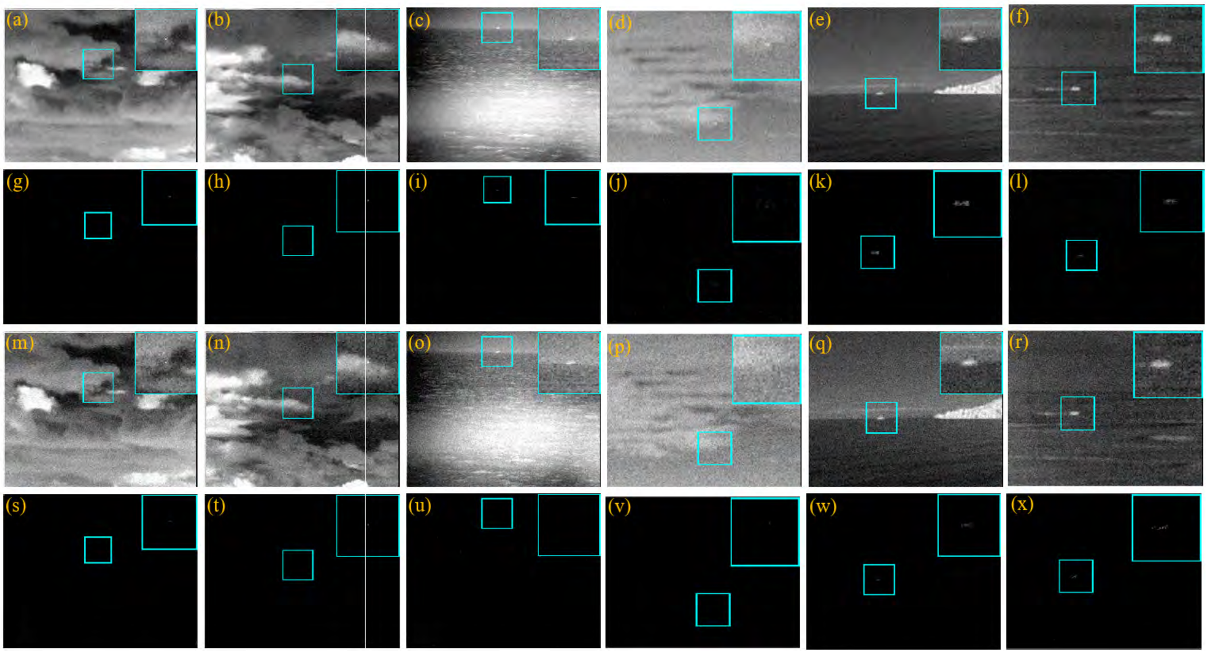

FIGURE 11. The images polluted by additive white Gaussian noise with standard deviation of 10 and 20 are shown in first and third rows, and the second and fourth rows present the detection results by the proposed algorithm.

100 images are randomly selected from Sequence 5, then each image is added with 4 different standard deviations of Gaussian white noise, in which standard deviations is 5, 10, 15, and 20, respectively. In this condition, these noise-added images can be divided into four groups based on noise intensity (denoted as NA-Groups 1-4). Subsequently, with the help of better denoising performance of nonlocally centralized sparse representation (NCSR) [57], it is employed to denoise the 4 groups of noise-added images. Then we obtain four corresponding groups of noise-removed images (denoted as NR-Groups 1-4). The proposed method is tested on NA-Groups 1-4 and NR-Groups 1-4. Fig. 12 shows the detection results of the proposed method on one image in each group of images. Table 5 gives the average probability of detection and false alarm rate obtained by the proposed method for the eight groups of images. From them, we can conclude that the higher the target contrast is, the easier it is to detect. The proposed algorithm can still function if the projected target could remain relatively salient in the local area of the contaminated image.

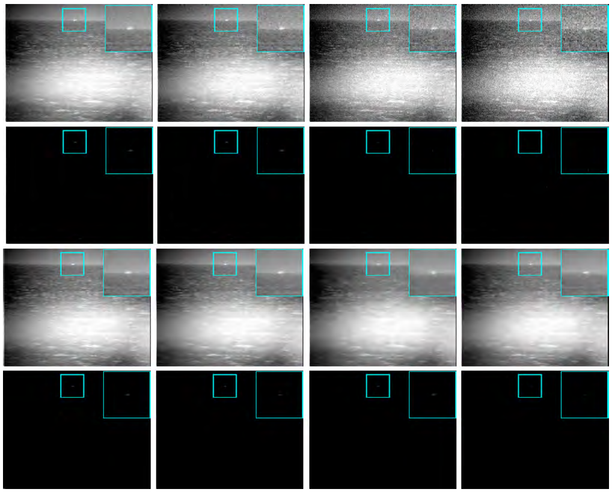

FIGURE 12. Detection results of the proposed method for the noisy image and the denoised image. Row 1: Noisy image with different noise level. Row 2: Detection results of noisy images. Row 3: Denoised images. Row 4: Detection results of denoised images.

VI. DISCUSSION OF THE PROPOSED METHOD

A. PARAMETER SETTINGS

In our proposed method, some critical parameters, such as the sparse penalty, graph regularization weight, low-rank approximation factor, patch size and sliding step, play key role in affecting the fitness of the proposed method for various real scenarios. These parameters can be selected experimentally. However, the empirical approach is time-consuming and hard to obtain the best detection performance due to lack of the criterion for quantitative evaluation. Nevertheless, we can narrow the scope of their choice in applications by analyzing the characteristics of different parameters.

1) SPARSE PENALTY λ_1

As a compromise between low-rank and sparse components, λ_1 is an important factor in optimization process. Although smaller sparse penalty can detect targets more steadily, it would cause high false alarm rate. Conversely, larger value can suppress strong clutter edge better, but it may reduce the intensity of small targets and even cause missing detection.

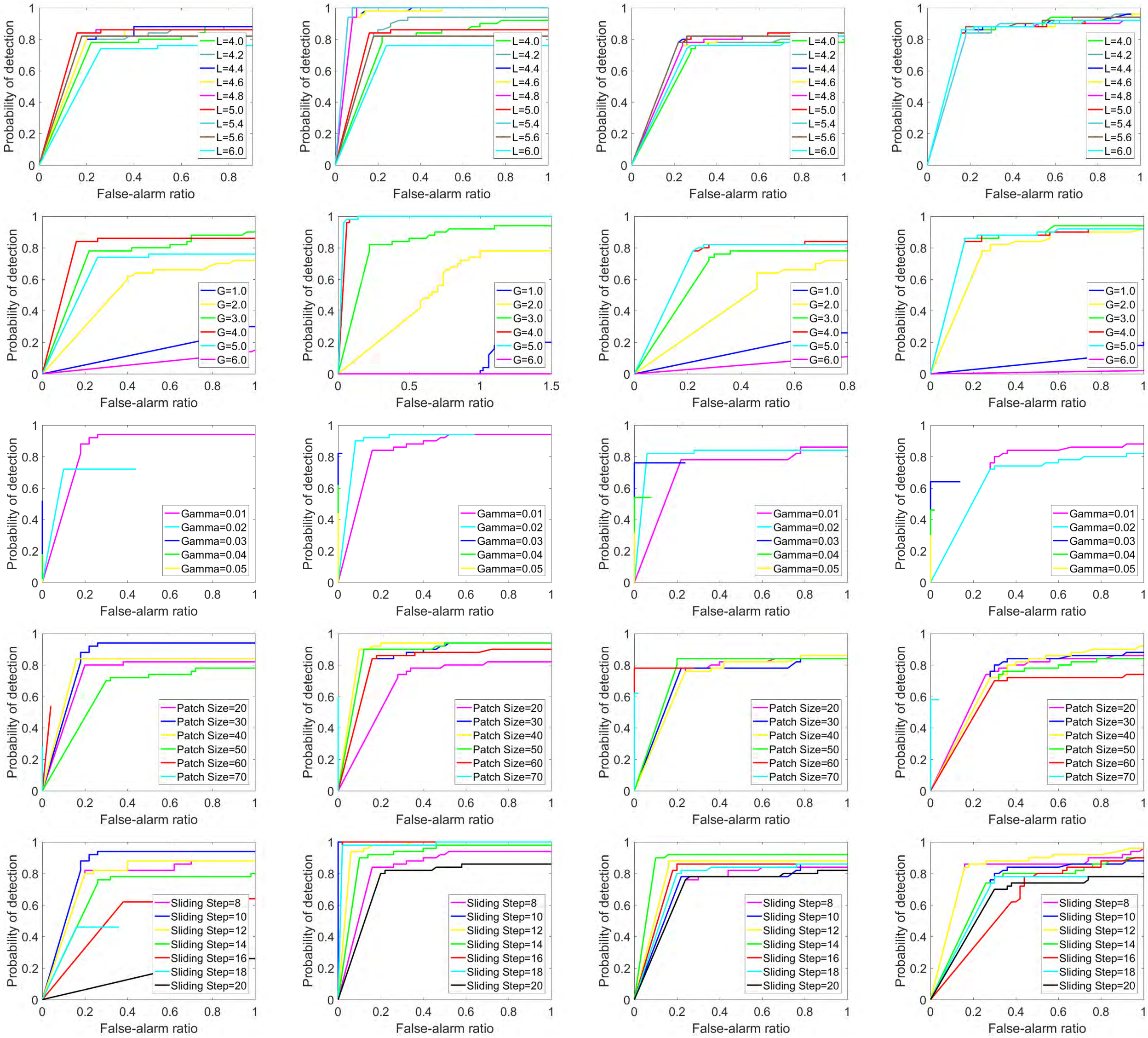

FIGURE 13. **ROC curves of detection results obtained tuning different parameters. Row 1: Different sparse penalties λ_1. Row 2: Different graph regularization weight λ_2. Row 3: Different approximation factors γ. Row 4: Different patch size. Row 5: Different sliding steps.**

For simplicity in testing, we use $\lambda_1 = L/\sqrt{\max(m, n)}$ as a substitute of the sparse penalty λ_1 and vary L from 4 to 6 with 0.2 interval. In the first row of Fig. 13, the ROC curves of different L on Sequences 1-4 are given. From the figures, it can be observed that the performance of the proposed method changes little in the intervals. Nevertheless, when L is too large, the detection performance is unsatisfactory, especially in Sequence 2. In our paper, we set L in [4, 6] in the following experiments.

2) GRAPH REGULARIZATION WEIGHT λ_2

It controls the weight's preservation degree to local structure of background. Generally, the larger the weight of graph regularization is, the less the background residuals are left in the target image. But it may result in missing detection in the case of overlarge weight, reducing the detection probability. To tune the parameter finely, we take λ_2 as $G/\sqrt{\min(m, n)}$, instead of directly varying λ_2. The second row of Fig. 13 presents the effect of λ_2 with different G. From the illustration, it finds that the detection rate of the proposed method would be reduced for over large or over small λ_2. For instance, the detection probability of $G = 1$ and $G = 6$ are low in Sequences 1-4. The detection results of G within [2,5] is acceptable. But $G = 2$ perform unstable compared with $G = 3, 4, 5$ among all tested sequences. In order to adapt to different scenarios better, we set G within the interval [3,5].

3) LOW-RANK APPROXIMATION FACTOR γ

Despite the usage of graph regularization weight, γ is also a critical parameter to control low-rank approximation. For Laplace norm, a smaller γ provides better approximation for true background (as illustrated in Fig.1(b)). However,

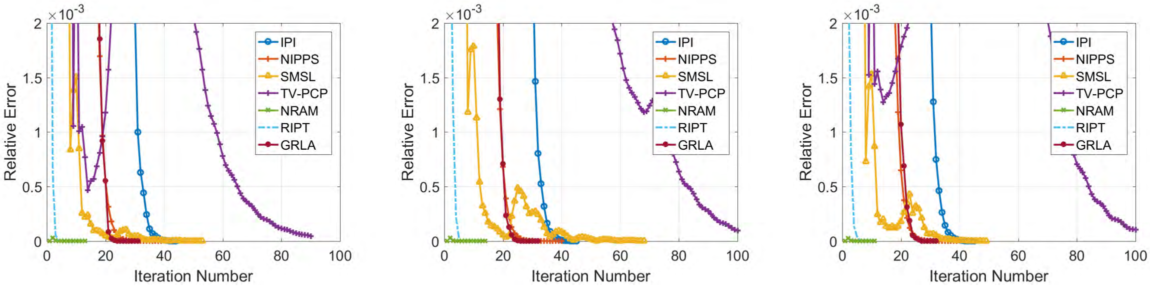

(a) (b) (c)

FIGURE 14. Convergence rates of the methods based on low-rank recovery.

TABLE 5. The average running time (/s) of each frame in Sequences 1-6.

Methods	Complexity	Seq. 1	Seq. 2	Seq. 3	Seq. 4	Seq. 5	Seq. 6
ILCM	O(L^3MN)	0.017	0.016	0.018	0.015	0.020	0.011
MPCM	O(L^3MN)	0.023	0.023	0.024	0.21	0.024	0.016
WLDM	O(L^3MN)	0.740	0.728	0.765	0.735	1.266	0.721
LSM	O(L^3MN)	0.019	0.021	0.018	0.017	0.018	0.012
IPI	O(Imn^2)	13.645	14.266	12.748	11.106	17.431	2.455
NIPPS	O(Imn^2)	6.287	6.189	6.654	6.213	6.596	2.372
TV-PCP	O(Imn^2)	140.473	141.249	137.578	149.844	141.664	63.191
SMSL	O(Imn)	0.366	0.351	0.309	0.335	0.261	0.145
NRAM	O(Imn^2)	2.809	2.722	2.907	2.821	3.242	1.037
RIPT	O(Imn^2)	1.045	1.332	1.262	0.976	1.962	0.674
GRLA	O($mn(log(n) + In)$)	**3.864**	**3.954**	**4.105**	**3.692**	**3.421**	**1.948**

when the factor is over small, it will wipe out some targets. Therefore, fine tuning of the factor is also significant. To more intuitively verify the impact of γ, we vary γ from 0.01 to 0.05 with 0.01 interval and show the ROC curves of their detection results in third row of Fig. 13. From the figures, it is easy to find that although $\gamma = 0.3, 0.4, 0.5$ keep the false alarm very low, their detection probability is also low. The detection performance of the algorithm gradually increases with the decrease of $\gamma = 0.01$ seems a better choice for Sequences 1-4 since it achieves the most stable detection performance.

4) PATCH SIZE

Patch size has a significant impact on the computational complexity and detection performance. A smaller patch size reduces the computational effort while lessening the target sparsity. Conversely, a larger patch size ensures the target sparser but also increases the sparsity of rare structure. In order to balance the computational burden and detection performance, we test our proposed method on different patch size within the scope of [20,70] with ten intervals. The fourth row of Fig. 13 shows the ROC curves. Observing the figures, we find that the detection result of patch size among [20,60] is acceptable. But when patch size increases to 70, the proposed method performs worst. Taking all these into account, we choose 30 as patch size because of its best robustness in all tested sequences.

5) SLIDING STEP

The sliding step influences the computational complexity and detection performance as well, which has a similar effect to the patch size. That is, a large sliding step also reduces the computational complexity and target sparsity, but the detection performance will be degraded if the sliding step is too large. To validate its role, the sliding steps changing from 8 to 20 at intervals of 2 are tested on our experiments. We display the ROC curves in the fifth row of Fig. 13. As shown in the figures, it can be observed that with the increase of step size, the detection performance decreases gradually. However, when the step size is too small, it not only does not improve the performance of the algorithm, but increases the computational complexity, such as sliding step 8. The best choice of sliding step is among 10 to 16, here we pick 12.

B. ALGORITHM CONVERGENCE AND COMPLEXITY

ADMM is employed to solve GRLA and G-GRLA model, which has been proved a $\mathcal{O}(1/k)$ convergence [58]. Therefore, our solving scheme is ensured to converge. In Fig. 14, we experimentally plot convergence curves of the proposed method and comparison methods based on low-rank recovery to evaluate their convergence. For comparison, when the relative error is less than 10^{-7}, the optimization iteration is stopped for all test methods. Besides, the maximum relative error in Fig. 14 is taken as 0.002 for convenient observation. From the figures, it easily finds that the convergence rate of the proposed method is faster than IPI, TV-PCP, NIPPS and SMSL, but slower than RIPT and NRAM. Furthermore, we briefly discuss the complexity of the proposed method. Given an $M \times N$ image, m, n are the rows and columns of the patch-image or mode-3 unfolding. For our proposed method, the complexity of graph construction needs $O(mnlog(n))$. The computational complexity of non-convex low-rank approximation depends on the number of final singular value decomposition, where the final SVD step is $O(Imn^2)$. So the overall complexity of our proposed method is $O(mn(log(n) + In))$, where I denotes the numbers of iterations. The computational complexity and average completion time of all tested methods for per frame in Sequences 1-6 are shown in Table 5. It is clearly that the saliency-based methods consume less time than the low-rank approximation methods, which is because most of time consuming is occupied by expensive SVD in every iteration for the low-rank approximation methods. Our proposed methods is faster than IPI, NIPPS and TV-PCP, but it takes more time than SMSL, NRAM and RIPT. Considering that the proposed method achieves the minimum false alarm and missing detection rate for different backgrounds, target types and target sizes, the proposed method is more desirable than other state-of-the-art ones.

VII. CONCLUSION

In this paper, we propose a novel infrared small target detection method that integrates Laplace low-rank approximation and graph regularization. Laplace norm is employed to further accurately recover the complex backgrounds with various types of clutters. For graph regularization, a nearest neighbor graph is constructed to mine the local structure of patch image. In addition, a sparse enhancement scheme including both reweighted l_1 norm and nonnegative constraints is introduced to suppress the non-target points. Furthermore, an ADMM-based optimization framework is used to solve the proposed method efficiently. Finally, we extend the proposed method to a general model via the substitution of different non-convex low-rank approximation functions. Experimental results on extensive real-world infrared images demonstrate the proposed method obtains favorable performance compared to the state-of-the-art methods. However, it is still difficult for our proposed method to effectively handle the case in which targets are completely submerged in cloud clutter or noise. The time consuming of the model is relatively expensive. Taking account of the above limitations, our future work will focus on how to better distinguish low contrast targets from background and explore new weighted schemes to reduce the execution time.

ACKNOWLEDGMENT

The authors would like to thank the editor and anonymous reviewers for their help comments and suggestions.

REFERENCES

[1] Y. Li and Y. Zhang, "Robust infrared small target detection using local steering kernel reconstruction," *Pattern Recognit.*, vol. 77, pp. 113–125, May 2018.

[2] S. Qi, J. Ma, C. Tao, C. Yang, and J. Tian, "A robust directional saliency-based method for infrared small-target detection under various complex backgrounds," *IEEE Geosci. Remote Sens. Lett.*, vol. 10, no. 3, pp. 495–499, May 2013.

[3] L. Dong, B. Wang, M. Zhao, and W. Xu, "Robust infrared maritime target detection based on visual attention and spatiotemporal filtering," *IEEE Trans. Geosci. Remote Sens.*, vol. 55, no. 5, pp. 3037–3050, May 2017.

[4] Y. Dai and Y. Wu, "Reweighted infrared patch-tensor model with both non-local and local priors for single-frame small target detection," *IEEE J. Sel. Topics Appl. Earth Observ. Remote Sens.*, vol. 10, no. 8, pp. 3752–3767, Aug. 2017.

[5] M. Rodriguez-Blanco and V. Golikov, "Multiframe GLRT-based adaptive detection of multipixel targets on a sea surface," *IEEE J. Sel. Topics Appl. Earth Observ. Remote Sens.*, vol. 9, no. 12, pp. 5506–5512, Dec. 2016.

[6] D. Liu, Z. Li, X. Wang, and J. Zhang, "Moving target detection by nonlinear adaptive filtering on temporal profiles in infrared image sequences," *Infr. Phys. Technol.*, vol. 73, pp. 41–48, Nov. 2015.

[7] C. Gao, L. Wang, Y. Xiao, Q. Zhao, and D. Meng, "Infrared small-dim target detection based on Markov random field guided noise modeling," *Pattern Recognit.*, vol. 76, pp. 463–475, Apr. 2018.

[8] K. Qian, H. Zhou, H. Qin, S. Rong, D. Zhao, and J. Du, "Guided filter and convolutional network based tracking for infrared dim moving target," *Infr. Phys. Technol.*, vol. 85, pp. 431–442, Sep. 2017.

[9] C. Gao, D. Meng, Y. Yang, Y. Wang, X. Zhou, and A. G. Hauptmann, "Infrared patch-image model for small target detection in a single image," *IEEE Trans. Image Process.*, vol. 22, no. 12, pp. 4996–5009, Dec. 2013.

[10] D. Liu, L. Cao, Z. Li, T. Liu, and P. Che, "Infrared small target detection based on flux density and direction diversity in gradient vector field," *IEEE J. Sel. Topics Appl. Earth Observ. Remote Sens.*, vol. 11, no. 7, pp. 2528–2554, Jul. 2018.

[11] S. D. Deshpande, M. H. Er, R. Venkateswarlu, and P. Chan, "Max-mean and max-median filters for detection of small-targets," *Proc. SPIE*, vol. 3809, pp. 74–83, Oct. 1999.

[12] T.-W. Bae, F. Zhang, and I.-S. Kweon, "Edge directional 2D LMS filter for infrared small target detection," *Infr. Phys. Technol.*, vol .55, no. 1, pp. 137–145, Jan. 2012.

[13] M. Zeng, J. Li, and Z. Peng, "The design of Top-hat morphological filter and application to infrared target detection," *Infr. Phys. Technol.*, vol. 48, no. 1, pp. 67–76, Apr. 2006.

[14] C. L. P. Chen, H. Li, Y. Wei, T. Xia, and Y. Y. Tang, "A local contrast method for small infrared target detection," *IEEE Trans. Geosci. Remote Sens.*, vol. 52, no. 1, pp. 574–581, Jan. 2014.

[15] Y. Qin and B. Li, "Effective infrared small target detection utilizing a novel local contrast method," *IEEE Geosci. Remote Sens. Lett.*, vol. 13, no. 12, pp. 1890–1894, Dec. 2016.

[16] J. Gao, Y. Guo, Z. Lin, W. An, and J. Li, "Robust infrared small target detection using multiscale gray and variance difference measures," *IEEE J. Sel. Topics Appl. Earth Observ. Remote Sens.*, vol. 11, no. 12, pp. 5039–5052, Dec. 2018.

[17] H. Deng, X. Sun, M. Liu, C. Ye, and X. Zhou, "Small infrared target detection based on weighted local difference measure," *IEEE Trans. Geosci. Remote Sens.*, vol. 54, no. 7, pp. 4204–4214, Jul. 2016.

[18] Y. Chen and Y. Xin, "An efficient infrared small target detection method based on visual contrast mechanism," *IEEE Geosci. Remote Sens.*, vol. 13, no. 7, pp. 962–966, Jul. 2016.

[19] X. Bai and Y. Bi, "Derivative entropy-based contrast measure for infrared small-target detection," *IEEE Trans. Geosci. Remote Sens.*, vol. 56, no. 4, pp. 2452–2466, Apr. 2018.

[20] H. Deng, X. Sun, M. Liu, C. Ye, and X. Zhou, "Infrared small-target detection using multiscale gray difference weighted image entropy," *IEEE Trans. Aerosp. Electron. Syst.*, vol. 52, no. 1, pp. 60–72, Feb. 2016.

[21] E. Candès, X. Li, Y. Ma, and J. Wright, "Robust principal component analysis?" *J. ACM*, vol. 58, no. 3, p. 11, May 2011.

[22] H. Peng, B. Li, H. Ling, W. Hu, W. Xiong, and S. J. Maybank, "Salient object detection via structured matrix decomposition," *IEEE Trans. Pattern Anal. Mach. Intell.*, vol. 39, no. 4, pp. 818–832, Apr. 2017.

[23] X. Liu, G. Zhao, J. Yao, and C. Qi, "Background subtraction based on low-rank and structured sparse decomposition," *IEEE Trans. Image Process.*, vol. 24, no. 8, pp. 2502–2514, Aug. 2015.

[24] H. Wang, Y. Cen, Z. He, Z. He, R. Zhao, and F. Zhang, "Reweighted low-rank matrix analysis with structural smoothness for image denoising," *IEEE Trans. Image Process.*, vol. 27, no. 4, pp. 1777–1792, Apr. 2018.

[25] N. Shahid, V. Kalofolias, X. Bresson, M. Bronstein, and P. Vandergheynst, "Robust principal component analysis on Graphs," in *Proc. IEEE Int. Conf. Comput. Vis. (ICCV)*, Dec. 2015, pp. 2812–2820.

[26] Z. Zhang and K. Zhao, "Low-rank matrix approximation with manifold regularization," *IEEE Trans. Pattern Anal. Mach. Intell.*, vol. 35, no. 7, pp. 1717–1729, Jul. 2013.

[27] S. Boyd, N. Parikh, E. Chu, B. Peleato, and J. Eckstein, "Distributed optimization and statistical learning via the alternating direction method of multipliers," *Found. Trends Mach. Learn.*, vol. 3, no. 1, pp. 1–122, Jul. 2011.

[28] S. Gaïffas and G. Lecué, "Weighted algorithms for compressed sensing and matrix completion," Jul. 2011, *arXiv:1107.1638*. [Online]. Available: https://arxiv.org/abs/1107.1638

[29] X. Bai and F. Zhou, "Analysis of new top-hat transformation and the application for infrared dim small target detection," *Pattern Recognit.*, vol. 43, no. 6, pp. 2145–2156, Jun. 2010.

[30] J. Han, Y. Ma, B. Zhou, F. Fan, K. Liang, and Y. Fang, "A robust infrared small target detection algorithm based on human visual system," *IEEE Geosci. Remote Sens. Lett.*, vol. 11, no. 12, pp. 2168–2172, Dec. 2014.

[31] S. Yao, Y. Chang, and X. Qin, "A coarse-to-fine method for infrared small target detection," *IEEE Geosci. Remote Sens. Lett.*, vol. 16, no. 2, pp. 256–260, Feb. 2019.

[32] Y. Wei, X. You, and H. Li, "Multiscale patch-based contrast measure for small infrared target detection," *Pattern Recogn.*, vol. 58, pp. 216–226, Oct. 2016.

[33] Y. Qin, L. Bruzzone, C. Gao, and B. Li, "Infrared small target detection based on facet kernel and random walker," *IEEE Trans. Geosci. Remote Sens.*, to be published.

[34] C. Xia, X. Li, and L. Zhao, "Infrared small target detection via modified random walks," *Remote Sens.*, vol. 10, no. 12, p. 2004, Dec. 2018.

[35] X. Liu, T. Yang, and J. Li, "Real-time ground vehicle detection in aerial infrared imagery based on convolutional neural network," *Electronics*, vol. 7, no. 6, p. 78, Jun. 2018.

[36] X. Zhou, C. Yang, and W. Yu, "Moving object detection by detecting contiguous outliers in the low-rank representation," *IEEE Trans. Pattern Anal. Mach. Intell.*, vol. 35, no. 3, pp. 597–610, Mar. 2013.

[37] S. E. Ebadi and E. Izquierdo, "Foreground segmentation with tree-structured sparse RPCA," *IEEE Trans. Pattern Anal. Mach. Intell.*, vol. 40, no. 9, pp. 2273–2280, Sep. 2018.

[38] Y. Dai, Y. Wu, and Y. Song, "Infrared small target and background separation via column-wise weighted robust principal component analysis," *Infr. Phys. Technol.*, vol. 77, pp. 421–430, Jul. 2016.

[39] X. Wang, Z. Peng, D. Kong, P. Zhang, and Y. He, "Infrared dim target detection based on total variation regularization and principal component pursuit," *Image Vis. Comput.*, vol. 63, pp. 1–9, Jul. 2017.

[40] T. Zhang, H. Wu, Y. Liu, L. Peng, C. Yang, and Z. Peng, "Infrared small target detection based on non-convex optimization with Lp-norm constraint," *Remote Sens.*, vol. 11, no. 5, p. 559, Mar. 2019.

[41] Y. Dai, Y. Wu, Y. Song, and J. Guo, "Non-negative infrared patch-image model: Robust target-background separation via partial sum minimization of singular values," *Infr. Phys. Technol.*, vol. 81, pp. 182–194, Mar. 2017.

[42] L. Zhang, L. Peng, T. Zhang, S. Cao, and Z. Peng, "Infrared small target detection via non-convex rank approximation minimization joint $l_{2,1}$ norm," *Remote Sens.*, vol. 10, no. 11, p. 1821, Nov. 2018.

[43] L. Zhang and Z. Peng, "Infrared small target detection based on partial sum of the tensor nuclear norm," *Remote Sens.*, vol. 11, no. 4, p. 382, Feb. 2019.

[44] Y. Sun, J. Yang, Y. Long, Z. Shang, and W. An, "Infrared patch-tensor model with weighted tensor nuclear norm for small target detection in a single frame," *IEEE Access*, vol. 6, pp. 76140–76152, 2018.

[45] Y. He, M. Li, J. Zhang, and Q. An, "Small infrared target detection based on low-rank and sparse representation," *Infr. Phys. Technol.*, vol. 68, pp. 98–109, Jan. 2015.

[46] X. Wang, Z. Peng, D. Kong, and Y. He, "Infrared dim and small target detection based on stable multisubspace learning in heterogeneous scene," *IEEE Trans. Geosci. Remote Sens.*, vol. 55, no. 10, pp. 5481–5493, Oct. 2017.

[47] Y. Chen, Y. Guo, Y. Wang, D. Wang, C. Peng, and G. He, "Denoising of hyperspectral images using nonconvex low rank matrix approximation," *IEEE Trans. Geosci. Remote Sens.*, vol. 55, no. 9, pp. 5366–5380, Sep. 2017.

[48] E. J. Candès, M. B. Wakin, and S. P. Boyd, "Enhancing sparsity by reweighted l_1 minimization," *J. Fourier Anal. Appl.*, vol. 14, nos. 5–6, pp. 877–905, Dec. 2008.

[49] M. Belkin and P. Niyogi, "Laplacian eigenmaps and spectral techniques for embedding and clustering," in *Advances in Neural Information Processing System*, vol. 14. Cambridge, MA, USA: MIT Press, 2002, pp. 585–591.

[50] J.-F. Cai, E. J. Candès, and Z. Shen, "A singular value thresholding algorithm for matrix completion," *SIAM J. Optim.*, vol. 20, no. 4, pp. 1956–1982, Mar. 2010.

[51] C. Lu, J. Tang, S. Yan, and Z. Lin, "Nonconvex nonsmooth low rank minimization via iteratively reweighted nuclear norm," *IEEE Trans. Image Process.*, vol. 25, no. 2, pp. 829–839, Feb. 2016.

[52] Y. Xie, Y. Qu, D. Tao, W. Wu, Q. Yuan, and W. Zhang, "Hyperspectral image restoration via iteratively regularized weighted schatten p-norm minimization," *IEEE Trans. Geosci. Remote Sens.*, vol. 54, no. 8, pp. 4642–4659, Aug. 2016.

[53] Z. Xu, X. Chang, F. Xu, and H. Zhang, "$L_{1/2}$ regularization: A thresholding representation theory and a fast solver," *IEEE Trans. Neural Netw. Learn. Syst.*, vol. 23, no. 7, pp. 1013–1027, Jul. 2012.

[54] Z. Kang, C. Peng, and Q. Cheng, "Robust subspace clustering via tighter rank approximation," in *Proc. 24th ACM Int. Conf. Inf. Knowl. Manage.*, Oct. 2015, pp. 393–401.

[55] Z. Kang, C. Peng, and Q. Cheng, "Robust PCA via nonconvex rank approximation," in *Proc. IEEE Int. Conf. Data Mining*, Nov. 2015, pp. 211–220.

[56] P. D. Tao and L. T. H. An, "Convex analysis approachto D.C. programming: Theory, algorithms and applications," *Acta Math. Vietnamica*, vol. 22, no. 1, pp. 289–355, Jan. 1997.

[57] W. Dong, L. Zhang, G. Shi, and X. Li, "Nonlocally centralized sparse representation for image restoration," *IEEE Trans. Image Process.*, vol. 22, no. 4, pp. 1620–1630, Apr. 2013.

[58] B. He and X. Yuan, "On the $O(1/n)$ convergence rate of the Douglas–Rachford alternating direction method," *SIAM J. Numer. Anal. (SIAM)*, vol. 50, no. 2, pp. 700–709, Apr. 2012.

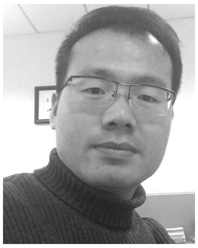

FEI ZHOU received the M.S. degree in electronic engineering from Xinjiang University, in 2017. He is currently pursuing the Ph.D. degree with the College of Electronic and Information Engineering, Nanjing University of Aeronautics and Astronautics. His research interests include image processing, target detection, and machine learning.

YIQUAN WU received the B.S. degree in instrumentation and test system from the Nanjing University of Aeronautics and Astronautics (NUAA), in 1984, and the M.S. and Ph.D. degrees in signal and information processing from NUAA, in 1987 and 1998, respectively, where he is currently a Professor and a Ph.D. Supervisor with the Department of Information and Communication Engineering, and he is involved in teaching and research in image processing and recognition, target detection and tracking, and intelligent information processing.

YIMIAN DAI received the B.S. degree in information engineering from the Nanjing University of Aeronautics and Astronautics (NUAA), Nanjing, China, in 2013, where he is currently pursuing the Ph.D. degree in signal and information processing. His current interests include target detection, image restoration, and machine learning.

PENG WANG received the B.E. and Ph.D. degrees from the College of Information and Communications Engineering, Harbin Engineering University, Harbin, China, in 2012 and 2018, respectively. In 2016, he was a Visiting Ph.D. Student with the Grenoble Images Parole Signals Automatics Laboratory (GIPSA-Lab), Grenoble Institute of Technology, Saint Martin d Heres, France. He is currently a Lecturer with the College of Electronic and Information Engineering, Nanjing University of Aeronautics and Astronautics, Jiangsu, China. His research interest includes hyperspectral imagery processing.

KANG NI is currently pursuing the Ph.D. degree with the School of Electronic and Information Engineering, Nanjing University of Aeronautics and Astronautics. His research interests include computer vision, pattern recognition, and scene classification.

• • •